

# Measurement of seismometer misorientation based on P-wave polarization: application to dense temporary broadband seismic array in the epicentral region of 2016 Gyeongju earthquake, South Korea

Min-Seong Seo<sup>1</sup>, Young Oh Son<sup>1</sup>, YoungHee Kim<sup>1\*</sup>, Tae-Seob Kang<sup>2</sup>, Junkee Rhie<sup>1</sup>, Kwang-Hee Kim<sup>3</sup>, and Jin-Han Ree<sup>4</sup>

<sup>1</sup>School of Earth and Environmental Sciences, Seoul National University, Seoul 08826, Republic of Korea

<sup>2</sup>Division of Earth Environmental System Science, Pukyong National University, Busan 48513, Republic of Korea

<sup>3</sup>Department of Geological Sciences, Pusan National University, Busan 46241, Republic of Korea

<sup>4</sup>Department of Earth and Environmental Sciences, Korea University, Seoul 02841, Republic of Korea

**ABSTRACT:** In this study, we probe the misalignment of 200 temporary broadband seismometers based on the polarization of *P* waves from regional and teleseismic earthquakes. The seismometers were deployed in the epicentral region of 2016  $M_L$  5.8 Gyeongju earthquake, South Korea, and this unprecedented dense array provided a unique opportunity for investigating fault structures from microseismicity. For the full use of three-component seismic records, we estimate and provide time-dependent misorientation angles of the 200 seismometers from June 2018 to March 2021 with uncertainty assessments. Two methods based on the principal component analysis and the minimization of transverse *P*-wave energy are applied. Our estimates are characterized by small uncertainty (average median absolute deviation of 3.14°). Moreover, periods of suspected temporal changes in misorientation angles mostly coincide with periods of reported technical operations, which demonstrates reliability of our methods to precisely detect the temporal variation of misorientation angles. We expect our misorientation angles to serve as an essential metadata for further seismological researches utilizing the dense array data.

**Key words:** seismometer misorientation, *P*-wave polarization, change point detection, receiver function analysis, 2016 Gyeongju earthquake

Manuscript received September 3, 2021; Manuscript accepted December 18, 2021

## 1. INTRODUCTION

Seismometer orientation is an essential information which must be accurately known to carry out modern seismological researches that utilize three-component seismograms including moment tensor inversion (e.g., Zahradník and Custódio, 2012),

receiver function analysis (e.g., Shen et al., 2019), shear wave splitting (e.g., Liu and Gao, 2013), and earthquake early warning (e.g., Eisermann et al., 2015). If it is unknown or incorrectly provided, the results of seismological analyses can be significantly biased and hence lead to incorrect inference from the results (e.g., Zahradník and Custódio, 2012; Zeng et al., 2020). A possible strategy to avoid such problems is to only use the data from seismic stations whose orientations are well known (e.g., Kim et al., 2010), but this limits a scope of seismic studies by not fully utilizing all available data. In fact, horizontal components recorded at borehole and ocean bottom seismometers are commonly misaligned from the geographic north and east, so the correction of such sensor misalignment has become a routine procedure that is proceeded before any seismic analysis (e.g., Shin et al., 2009; Lim et al., 2018).

### \*Corresponding author:

YoungHee Kim

School of Earth and Environmental Sciences, Seoul National University, 1 Gwanak-ro, Gwanak-gu, Seoul 08826, Republic of Korea  
Tel: +82-2-880-6735, E-mail: youngkim@snu.ac.kr

### Electronic supplementary material

The online version of this article (<https://doi.org/10.1007/s12303-021-0041-3>) contains supplementary material, which is available to authorized users.

from seismic records. Some of these methods include measuring *P*-wave polarization (Shin et al., 2009; Niu and Li, 2011; Lee and Sheen, 2015; Wang et al., 2016; Scholz et al., 2017; Ensing and van Wijk, 2018; Ojo et al., 2019; Braunmiller et al., 2020; Xu et al., 2020; Zeng et al., 2020; Zhu et al., 2020; Büyükkapınar et al., 2021; Son et al., 2021), measuring Rayleigh-wave polarization (Laske et al., 1994; Stachnik et al., 2012; Rueda and Mezcua, 2015; Doran and Laske, 2017; Scholz et al., 2017; Ojo et al., 2019; Xu et al., 2020; Zhu et al., 2020; Büyükkapınar et al., 2021), comparing observed and synthetic surface wave seismograms (Ekström and Busby, 2008; Ekström and Nettles, 2018; Braunmiller et al., 2020), measuring ambient noise cross-correlation (Zha et al., 2013; Lee and Rhie, 2015; Ensing and van Wijk, 2018; Xu et al., 2018; Zeng et al., 2020), and calculating receiver function (Lim et al., 2018; Zheng et al., 2020). Among these methods, calculation of synthetic seismograms or ambient noise cross-correlation can be relatively expensive in terms of computational cost. Moreover, ambient noise cross-correlation method is known to be less susceptible to structural effects owing to small interstation ray path, but the method requires temporally long enough data for which the orientation was fixed (Zha et al., 2013). As we will show in the Section 5.1, the stations which we analyzed experienced multiple changes in orientation, so it is difficult to *a priori* select time period for extracting the cross-correlation function. Measurement of Rayleigh-wave polarization can be advantageous in terms of data number due to relatively high signal-to-noise ratio (SNR) of Rayleigh waves, but the uncertainty levels are typically higher than that of *P*-wave polarization measurements (Scholz et al., 2017; Büyükkapınar et al., 2021). Although the *P*-wave polarization is potentially susceptible to anisotropic effect, such an effect can be minimized if a sufficiently large number of earthquakes are used in determining the orientation of two horizontal components of any particular station. Therefore, in constraining the sensor orientation, we select the method based on *P*-wave polarization that is computationally cost-effective as well as provides the high accuracy of the estimates.

Gyeongju Hi-density Broadband Seismic Network (GHBSN) is the largest ever dense array in South Korea, consisting of 200 broadband seismometers, that was deployed in the epicentral region of 2016  $M_L$  5.8 Gyeongju earthquake for the purpose of monitoring microseismicity and evaluating seismic hazard of a critical structure such as Wolsong nuclear power plant (Lim et al., 2021; Fig. 1a). All 200 stations are surface stations, so it is expected that the horizontal components of the stations should be generally well aligned. However, field measurements conducted in November 2020 showed that 73 out of 193 stations (N008–N200) were in fact misaligned by angles greater than 10°. Such substantial misalignments can impact results of seismic analyses utilizing horizontal-component seismograms, leading to incorrect

tectonic interpretation from the results.

In this study, we first estimated misorientation angles for full operation period of the GHBSN up to March 2021 by using two different methods (denoted as  $P_{PCA}$  and  $P_{min\ T}$ ), both based on the *P*-wave polarization. We then designed and employed a semi-automatic routine that can accurately detect the period corresponding to a change in the misorientation angle for a particular station. Based on this two-step procedure, we compiled a table that includes time-dependent misorientation angles for 200 stations in the GHBSN for its full operation period. We note that the same analysis procedure was performed for the data of permanent seismic networks in South Korea (Son et al., 2021). In this work, we validated our estimates first by showing improved interstation correlation between horizontal-component seismograms for teleseismic earthquakes after correcting for misalignment. Our misorientation angles are further assessed by examining amplitudes of the tangential-component receiver functions at 0 s before and after the correction.

## 2. DATA

The 200 stations (N001–N200; network code KH) were installed over an area of  $60 \times 60 \text{ km}^2$  with an average interstation distance of 4.5 km (Fig. 1a). They were deployed through four phases: 7 stations in phase I (completed in November 2017), 35 stations in phase II (completed in January 2019), 83 stations in phase III (completed in March 2019), and 75 stations in phase IV (completed in September 2019). The stations were equipped with Nanometrics Trillium Compact PH velocity sensors, recording the data at 200 samples per second (sps). Locations of 13 stations were changed more than once after the deployment till March 2021, and the rest of the stations kept their locations fixed. Also, several data gaps exist due to minor problems including battery discharge, but they were not significant to affect our analysis.

The *P*-wave polarization method requires *P*-wave signals of earthquakes with sufficiently high SNRs. We selected 1019 earthquakes with a moment magnitude ( $M_W$ ) exceeding 5.5 and with an epicentral distance ranging from 0° to 90° with respect to a location of 36.5°N, 128°E (Fig. 1b). To increase the computational efficiency of our analysis, we downsampled the data points from 200 sps to 20 sps. Furthermore, we removed the mean and trend of waveforms, and then applied cosine taper and zero-phase band-pass filter at the frequency range of 0.02–0.2 Hz. The frequency range of 0.02–0.2 Hz has been used for a number of previous studies that adopted *P*-wave polarization method to estimate misorientation angles, including the work applied to permanent seismic networks in South Korea (Son et al., 2021), and has proven to be successful (Niu and Li, 2011; Wang et al., 2016; Ojo et al., 2019; Zeng et al., 2020).

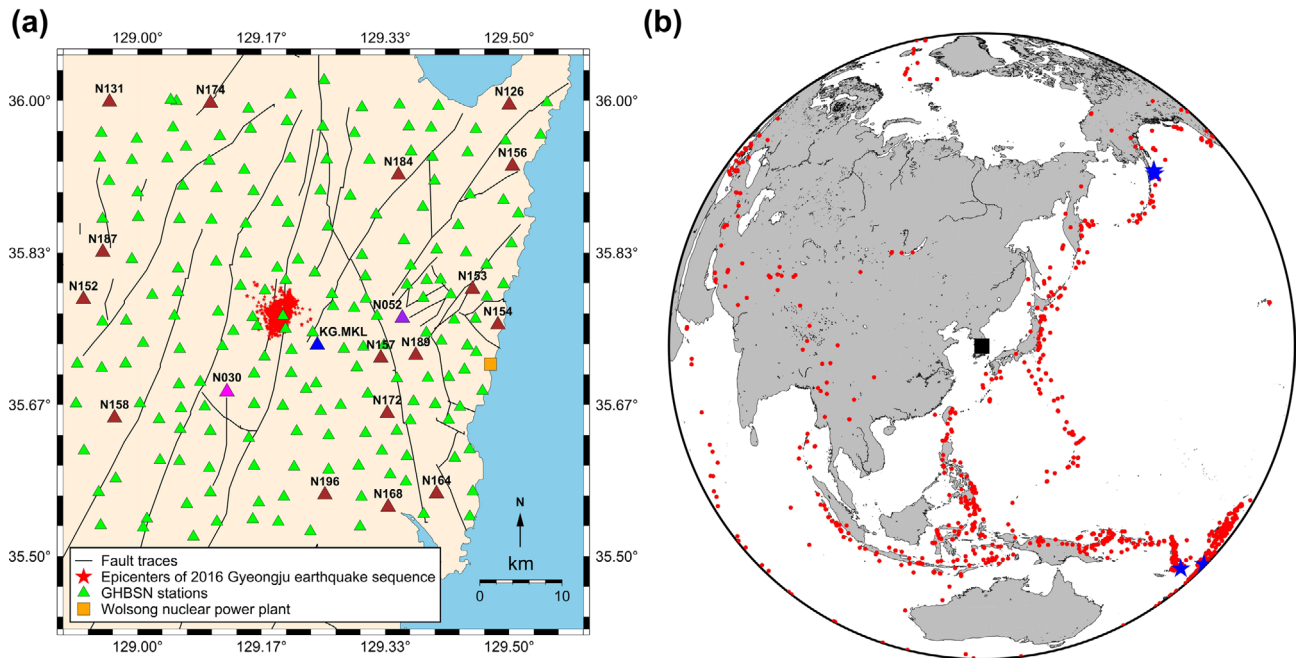


**Fig. 1.** (a) The map of 200 stations (N001–N200) of the GHBSN in southeastern part of the Korean Peninsula. Stations are marked as green triangles. Station MKL of KG network is marked as a blue triangle, station N030 is marked as a magenta triangle, station N052 is marked as a purple triangle, and Wolsong nuclear power plant is marked as an orange square. The 16 stations used for receiver function analysis are marked as dark brown triangles. Red stars indicate the epicenters of 2016 Gyeongju earthquake sequence relocated by Woo et al. (2019). The fault traces in the region (Kim et al., 2017) are plotted as black lines. (b) The map of 1019 earthquakes for which we measured  $P$ -wave polarization. Each event is marked as a red dot. Black square marks the reference location of 36.5°N, 128°E. Four blue stars represent the telesismic earthquakes listed in Table 1.

### 3. METHODS

We adopted the method applied by Son et al. (2021) to estimate misorientation angles of GHBSN stations. Following the convention adopted by Son et al. (2021), we defined misorientation angle  $\theta_M$  as shown in Figure 2. If the north-south sensor is rotated from the geographic north by  $\theta_M$ , the apparent back azimuth

measured from  $P$ -wave polarization is  $\theta_A$  while the theoretical back azimuth estimated from the station-event geometry is  $\theta_T$ . A misorientation angle  $\theta_M$  is then the difference between  $\theta_T$  and  $\theta_A$ . In Section 3.1, we summarize two  $P$ -wave-polarization-based methods to infer  $\theta_A$  from recorded seismograms. See Son et al. (2021) for detailed explanation of the methods.

#### 3.1. $P$ -wave Polarization Method

In the absence of anisotropic effects,  $P$  wave is polarized in the direction of propagation path. In light of such principle, the  $P_{PCA}$  method estimates the  $P$ -wave polarization directly by finding the dominant particle motion from recorded seismograms. We applied principal component analysis (PCA; Pearson, 1901) on three-component seismograms containing  $P$  wave. PCA finds the most influential component of multidimensional data by computing covariance matrix and calculating the eigenvector which corresponds to the largest eigenvalue. In context of our problem, the direction of such an eigenvector is equal to the direction of the dominant  $P$ -wave particle motion. Thus,  $\theta_A$  is directly obtained as the angle between the north-south component of sensor and the dominant particle motion direction as shown in Figure 3a.

The  $P_{min\ T}$  method also measures the  $\theta_A$  from the  $P$ -wave

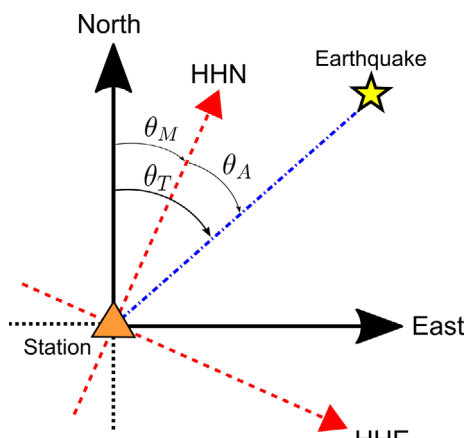


**Fig. 2.** Schematic description of misorientation angle ( $\theta_M$ ) from a station-earthquake geometry. If the north-south sensor is deviated from the geographic north by  $\theta_M$ ,  $\theta_M$  is equal to the difference between the apparent back azimuth ( $\theta_A$ ) and the theoretical back azimuth ( $\theta_T$ ). Adopted from Figure 2 of Son et al. (2021).

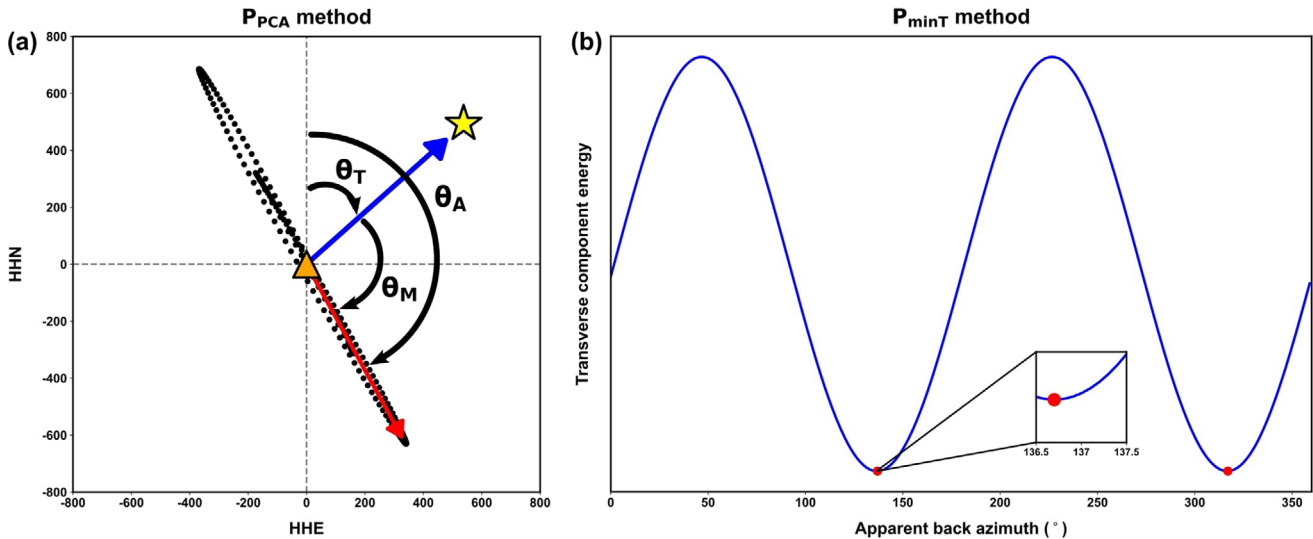


**Fig. 3.** Schematic diagrams describing (a)  $P_{PCA}$  method and (b)  $P_{minT}$  method. In panel (a), horizontal  $P$ -wave particle motion within the signal window is illustrated. Each data sample is marked by a black dot. Red arrow indicates the direction of apparent back azimuth calculated by PCA and blue arrow indicates the direction of theoretical back azimuth assuming that horizontal sensor is perfectly aligned. The angle between two arrows corresponds to the misorientation angle. A station and an event are marked as an orange triangle and a yellow star, respectively. In panel (b), the variation of transverse component energy measured within the  $P$ -wave signal window is shown with respect to apparent back azimuth. The transverse energy varies sinusoidally as a function of apparent back azimuth. Two red dots represent candidates of apparent back azimuth minimizing the transverse component energy by exactly  $180^\circ$ .

polarization characteristics, but it finds the angle which minimizes  $P$ -wave energy in the transverse component after rotating to vertical-radial-transverse (ZRT) coordinate system. We performed grid search by increasing candidate back azimuth from  $0^\circ$  to  $360^\circ$  and measured the transverse  $P$ -wave energy. There were two candidates of  $\theta_A$  which exactly differed by  $180^\circ$ , but we resolved such an ambiguity by selecting one that resulted in positive normalized zero-lag cross-correlation coefficient ( $CC_{min}$ ) between vertical and radial components. Grid search procedure adopted by the  $P_{minT}$  method is described in Figure 3b.

### 3.2. Quality Control Parameter Selection

To determine the misorientation angle for each station, we calculated median and mean of the measurements obtained from the individual events. However, we first performed the quality control so that only the high-quality measurements were retained. The parameters which we calibrated for the quality control are the length of the  $P$ -wave signal window, the SNR, the rectilinearity of the  $P$ -wave particle motion (recti  $P$ ) for the  $P_{PCA}$  method, and the  $CC_{min}$  for the  $P_{minT}$  method. We defined the SNR as ten times the logarithm of ratio between mean square amplitudes in the signal and noise windows (Shin et al., 2009). The recti  $P$  is a measure of the  $P$ -wave particle motion linearity and was calculated from the eigenvalues obtained by PCA following the definition of Jurkevics (1988). We followed the step-by-step procedure described in Son et al. (2021) to calibrate

each parameter.

First, to determine the optimal  $P$ -wave signal window, we predicted theoretical  $P$ -wave arrival time ( $T_p$ ) with global 1D velocity model (IASP91; Kennett and Engdahl, 1991). Considering the misfit between theoretical and observed  $P$ -wave arrivals, we searched for the optimal pair of time before and after  $T_p$  ( $t_{before}/t_{after}$ ). For this purpose, we defined the “reference station” whose misorientation angle was fixed for the whole observation period and the polarization measurements were of high quality. Specifically, we selected the stations which had more than 100 measurements, the median absolute deviation (MAD) of estimates was smaller than  $4^\circ$ , and the median of recti  $P/CC_{min}$  was greater than 0.98/0.95 ( $M_W \geq 6$  events were used for the selection), respectively. We counted the number of reference stations for every combination of  $t_{before}$  and  $t_{after}$  by varying each parameter from 1 s to 10 s and searched for the combination which maximized the number of reference stations.

After determining the optimal signal window, we searched for the optimal lower threshold of SNR. To determine this threshold, we calculated the median recti  $P/CC_{min}$  in the moving window of 10000 station-event pairs with 50% overlap, after sorting all pairs in ascending order by SNR. Since both recti  $P$  and  $CC_{min}$  increased with SNR, we chose the median SNR of the moving window whose median recti  $P/CC_{min}$  first exceeded 0.98/0.95 as the cutoff threshold, respectively. Afterward, we discarded the station-event pairs with SNR lower than the determined threshold and also the pairs with recti  $P/CC_{min}$

lower than 0.98/0.95, respectively. The parameter selection result is described in Section 4.1.

### 3.3. Monitoring Time-dependent Misorientation

To monitor possible time-dependent change in misorientation for each station, we applied change point detection method as also adopted by Son et al. (2021). First, given misorientation measurements that passed the quality criteria, we applied the pruned exact linear time (PELT) method (Killick et al., 2012) to divide time series of misorientation angles into segments of constant values. We then manually checked if the segmentation was properly performed and corrected for the false segmentations. We defined “validation period” as the segmented interval with constant misorientation. For stations with more than one month

of data gap within a validation period, we redefined the validation periods by dividing original period to subintervals so that substantial data gap is not included in each validation period.

We applied the segmentation procedure to misorientation measurements from  $P_{PCA}$  and  $P_{min\ T}$  methods for 200 stations to obtain validation periods. For every validation period, we then calculated median and trimmed mean as the representative estimates of misorientation angle, while MAD and trimmed standard deviation (trimmed SD) as the uncertainty estimates. To calculate trimmed mean and trimmed SD, we removed the outliers in the validation period whose values were outside [Median  $- 5 \times$  MAD, Median  $+ 5 \times$  MAD]. Figure 4 shows temporal variation of misorientation angles with two validation periods for station N052 (Fig. 1a), as an example, based on  $P_{PCA}$  and  $P_{min\ T}$  methods.

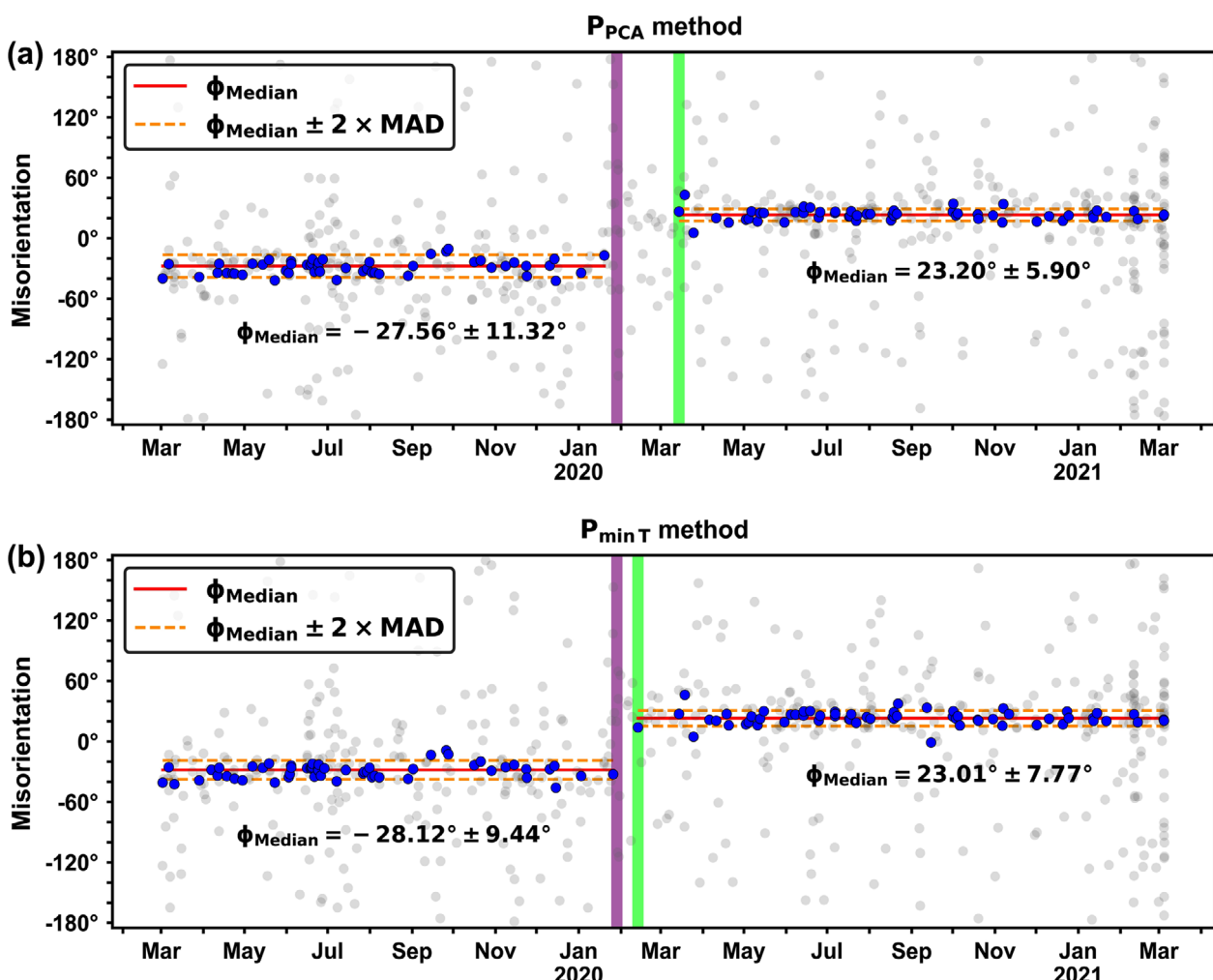


**Fig. 4.** Temporal variation of misorientation angles calculated by (a)  $P_{PCA}$  method and (b)  $P_{min\ T}$  method for station N052. Each dot corresponds to the misorientation angle calculated from a single earthquake. Blue dots are measurements which passed the quality criteria, described in Section 3.2, while grey dots are those which did not. Two panel figures show that assigned quality criteria are effective in removing poor-quality measurements with large scatter. A red solid line and orange dotted lines indicate the median and  $2 \times$  MAD of each validation period, respectively. A green vertical line denotes the timing of temporal change determined by our detection method and a purple vertical line denotes the timing of type II operation defined in Section 5.1.

## 4. RESULTS

### 4.1. Optimal Parameters for Quality Control

Following the procedure outlined in Section 3.2, we searched for the pairs of  $t_{\text{before}}$  and  $t_{\text{after}}$  which yield the maximum number of reference stations separately for the  $P_{\text{PCA}}$  and the  $P_{\min T}$  methods. For the  $P_{\text{PCA}}$  method, the optimal pair is  $(t_{\text{before}}, t_{\text{after}}) = (2 \text{ s}, 8 \text{ s})$  (Fig. 5a), and for the  $P_{\min T}$  the optimal pair is  $(t_{\text{before}}, t_{\text{after}}) = (3 \text{ s}, 8 \text{ s})$

(Fig. 5c). Similar parameter pairs obtained for two independent methods clearly indicate that signal windows required for the stable measurement of  $P$ -wave polarization are almost identical regardless of the method.

Figures 5b and d describe the procedure for SNR threshold determination. For the  $P_{\text{PCA}}$  and  $P_{\min T}$  methods, determined SNR thresholds were 11.77 dB and 11.68 dB, respectively. It is also visually confirmed from the figures that the misorientation values are less scattered as SNR increases beyond the determined

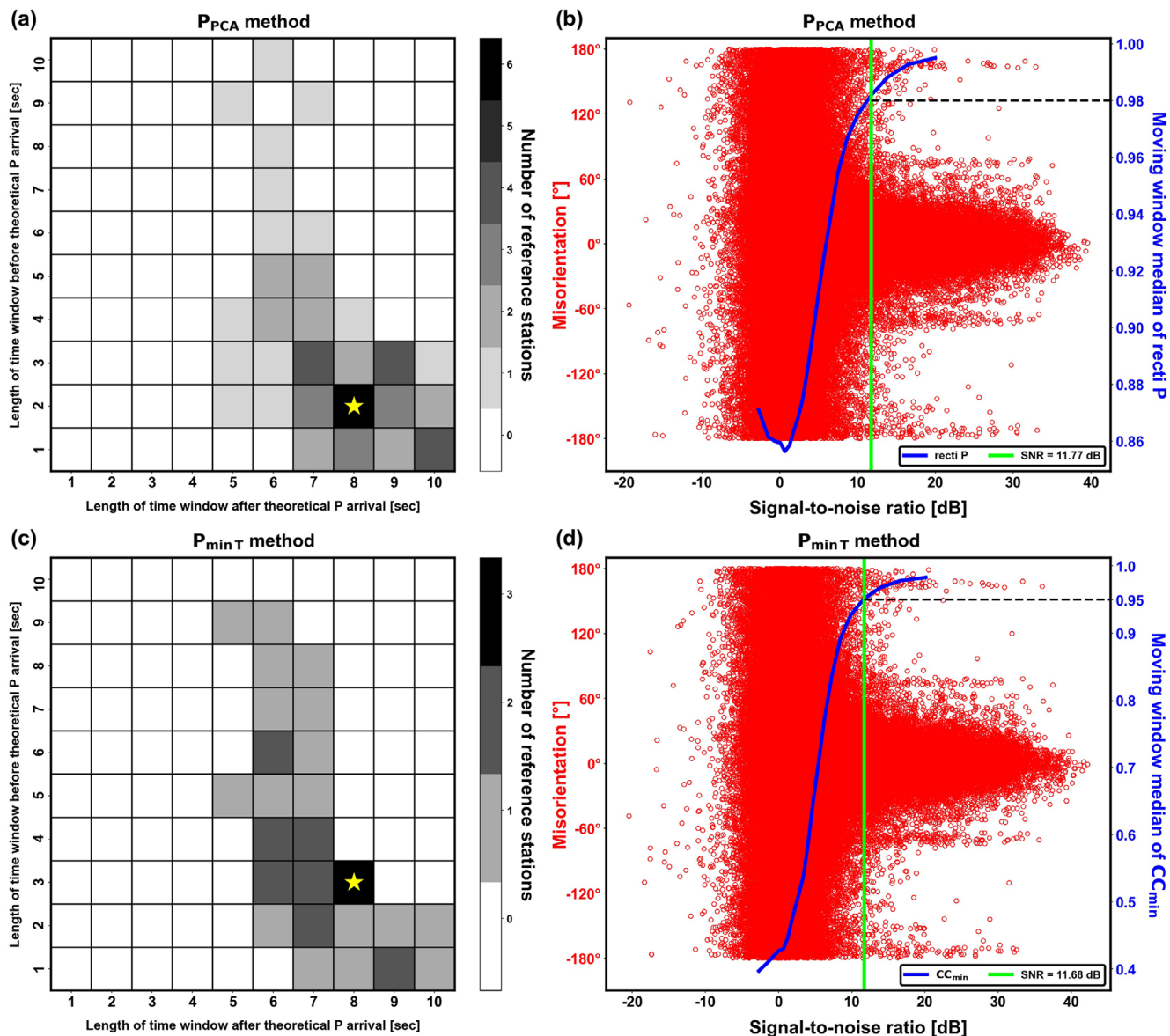


**Fig. 5.** (a and c) Heatmaps showing the number of reference stations for two methods. Parameter combinations for the maximum reference stations are  $(t_{\text{before}}, t_{\text{after}}) = (2 \text{ s}, 8 \text{ s})$  for (a)  $P_{\text{PCA}}$  method and  $(t_{\text{before}}, t_{\text{after}}) = (3 \text{ s}, 8 \text{ s})$  for (c)  $P_{\min T}$  method, which are marked as yellow stars. (b and d) Distribution of misorientation angles with respect to SNR with the median of recti  $P$  and  $\text{CC}_{\min}$  calculated by two methods. Each red dot corresponds to the misorientation angle calculated from a single event. Blue curves depict the median of (b) recti  $P$  and (d)  $\text{CC}_{\min}$  for 50% overlapping moving window with 10000 events, exceeding 0.98 and 0.95 when the median of SNR in the corresponding window is over 11.77 and 11.68, respectively. The misorientation angle range from  $-180^\circ$  to  $180^\circ$  since we subtracted  $360^\circ$  from the angles larger than  $180^\circ$  for the ease of plotting.

threshold, and this indeed indicates that the determined SNR thresholds are adequate values for filtering out the measurements of poor quality. To confirm that the specific choice of moving window and overlapping window lengths does not affect the SNR threshold value, we tested several window lengths and confirmed that the resulting SNR thresholds were similar to 11 dB in all cases. Therefore, we selected 11 dB as the final SNR threshold for both the  $P_{PCA}$  and  $P_{min T}$  methods.

#### 4.2. Statistics of the Misorientation Angles

Following the procedure described in Section 3.3, we compiled time-dependent misorientation angles for the two methods. We discarded validation periods which contained less than five measurements due to insufficient data number to estimate reliable representative misorientation angles corresponding to such periods. Wang et al. (2016) suggested 10 high-quality measurements as the minimum required number of measurements to obtain a stable misorientation value from the bootstrap analysis. However, we found that a number of validation periods with less than 10 measurements showed constant misorientation throughout the period. Therefore, we set the minimum required measurement number for the validation period as five. Additionally, we discarded validation periods with MAD larger than  $20^\circ$  (total of three) since we considered measurements are not reliable for those periods due to large uncertainty. We provide the table of estimated misorientation angles for the GHBSN (Table S1 in the electronic supplementary material). For the cases which  $P_{PCA}$  and  $P_{min T}$  methods yielded different segmentations, we chose the union of

validation periods from two methods as the final validation period.

We compared the misorientation estimates from the  $P_{PCA}$  and  $P_{min T}$  methods corresponding to each validation period. If our measurements are robust, we would expect high degree of correlation between the results obtained from two methods. Figure 6a demonstrates that there exists a high degree of correlation ( $R^2 = 0.999$ ) between the median estimates. In addition, we observe from Figure 6b that two different representative estimates (median and trimmed mean) calculated by the  $P_{PCA}$  method are also highly consistent ( $R^2 = 0.999$ ). The high degree of correlation ( $R^2 > 0.995$ ) was also found between the trimmed mean estimates ( $P_{PCA}/P_{min T}$ ) and the  $P_{min T}$  estimates (median/trimmed mean) (Fig. S1 in the electronic supplementary material). This altogether implies that our measurement results are consistent regardless of the choice of the method or the type of representative estimates (median/trimmed mean), and hence any value can be chosen for the misorientation correction in practice. We note that  $P_{min T}$  method requires grid search through candidate angles and hence can be more computationally intensive than  $P_{PCA}$  method which utilizes computationally efficient linear algebra library (e.g., Harris et al., 2020) for PCA analysis.

Figure 7a shows the distribution of misorientation angles and the associated errors (MADs) for 335 validation periods obtained from the  $P_{PCA}$  method. 98.52% of the misorientation angles are distributed within  $\pm 70^\circ$  with the average value of  $0.032^\circ$  (Fig. 7a). However, the standard deviation is  $17.10^\circ$  even after removing the measurements whose absolute values are larger than  $100^\circ$ . This is quite a large misalignment expected for surface seismometers,

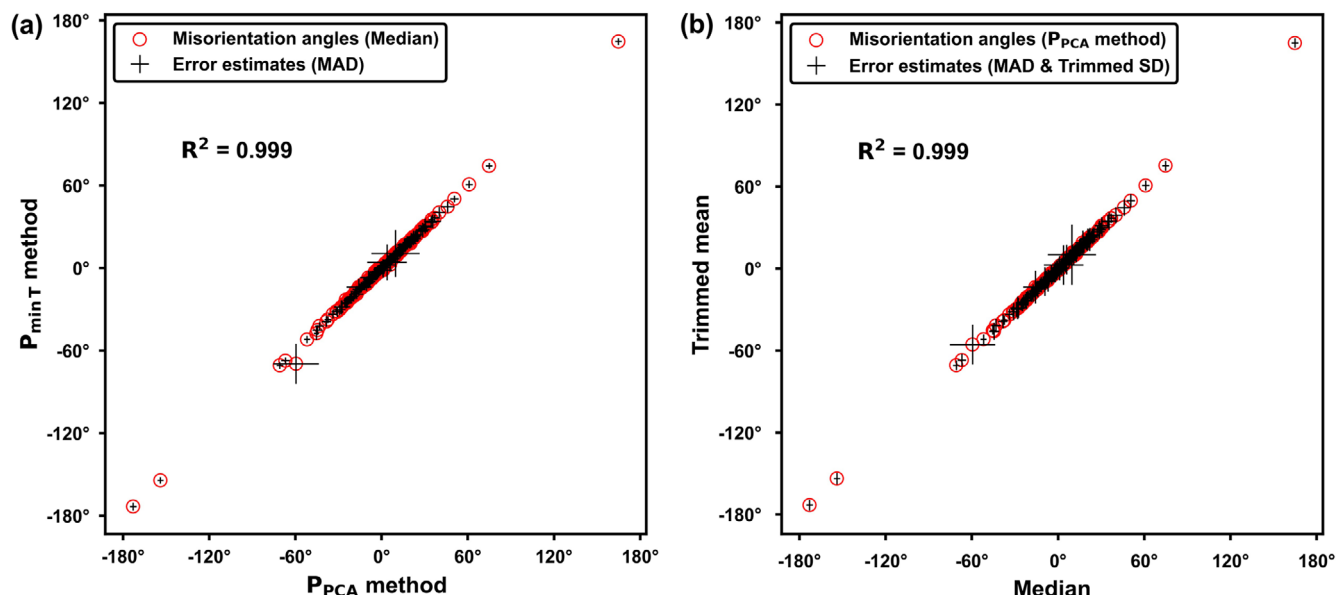


**Fig. 6.** (a) Comparison of median estimates for each validation period from the  $P_{PCA}$  and  $P_{min T}$  methods. Empty red circles are estimated misorientations for each validation period. (b) Comparison of median and trimmed mean estimates calculated from the  $P_{PCA}$  method.

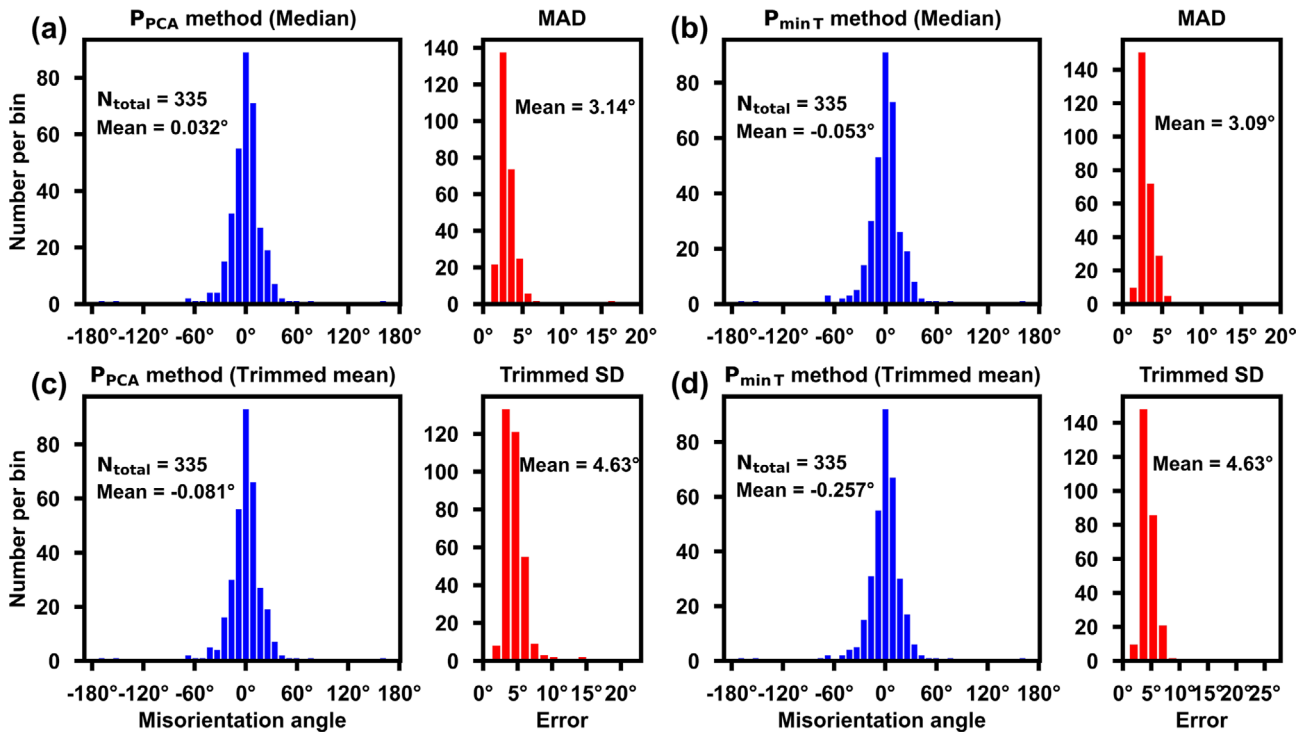


**Fig. 7.** (a) Left: Histogram of median estimates for 335 validation periods obtained from the  $P_{PCA}$  method. The mean of all estimates is  $0.032^\circ$ . Right: Histogram of MADs for 335 validation periods obtained from the  $P_{PCA}$  method. The mean of all MADs is  $3.14^\circ$ . (b-d) The analogous histograms for  $P_{minT}$  method (median/MAD),  $P_{PCA}$  method (trimmed mean/trimmed SD), and  $P_{minT}$  method (trimmed mean/trimmed SD).

because unlike borehole and ocean bottom seismometers, their orientations can be manually checked after the installation. Such large deviations from the geographic north and the east emphasize the importance of misorientation correction for seismometers in GHBSN before utilizing horizontal component records. Overall uncertainty estimate is very small, as the average MAD of estimates obtained from the  $P_{PCA}$  method is  $3.14^\circ$  and 98.22% of MAD values are less than  $10^\circ$ . The distribution of misorientation angles/errors are also similar for other cases (Figs. 7b–d) as was also confirmed in Figure 6.

## 5. DISCUSSION

### 5.1. Possible Cause for the Temporal Change of Sensor Misorientations

For 14 stations (Table S2 in the electronic supplementary material), validation periods were divided based on the start and end dates of data gaps. We thus need to detect changes in sensor orientation that are likely to be the results of genuine temporal change in order to discuss the possible origin of such changes. We assumed that the change between two consecutive validation periods was indicative for the change in sensor misalignment if the mean misorientation values did not overlap within each other's uncertainty range. With such assumption,

we concluded that 87 stations experienced substantial temporal change at least once with the total of 97 notable changes. We briefly discuss possible causes responsible for the considerable number of temporal changes that took place during the relatively short deployment period (< 3 years).

From the field report of GHBSN management, we identified three operation types that may have been responsible for the temporal misorientation change: station relocation (type I), sensor hole renovation with mortar casting (type II), and malfunction troubleshooting (type III). Among the 97 detected changes, we found 70 changes that are coincident with known operation records. In detail, we could associate 5 changes with type I, 61 changes with type II, and 4 changes with type III operation (Table S3 in the electronic supplementary material). Remaining 27 changes could not be matched with any known operation record, but we suspect these to be the result of undocumented operations. The overall status of misorientation angles for two different periods (October 1<sup>st</sup>, 2019 and February 1<sup>st</sup>, 2021) is shown in Figure S2 of the electronic supplementary material.

### 5.2. Validation by Interstation Cross-correlation Measurement of Teleseismic Seismograms

To validate our misorientation estimates, we calculated the cross-correlation coefficient (CC) between horizontal teleseismic

**Table 1.** The list of four teleseismic earthquakes used for the interstation cross-correlation measurements

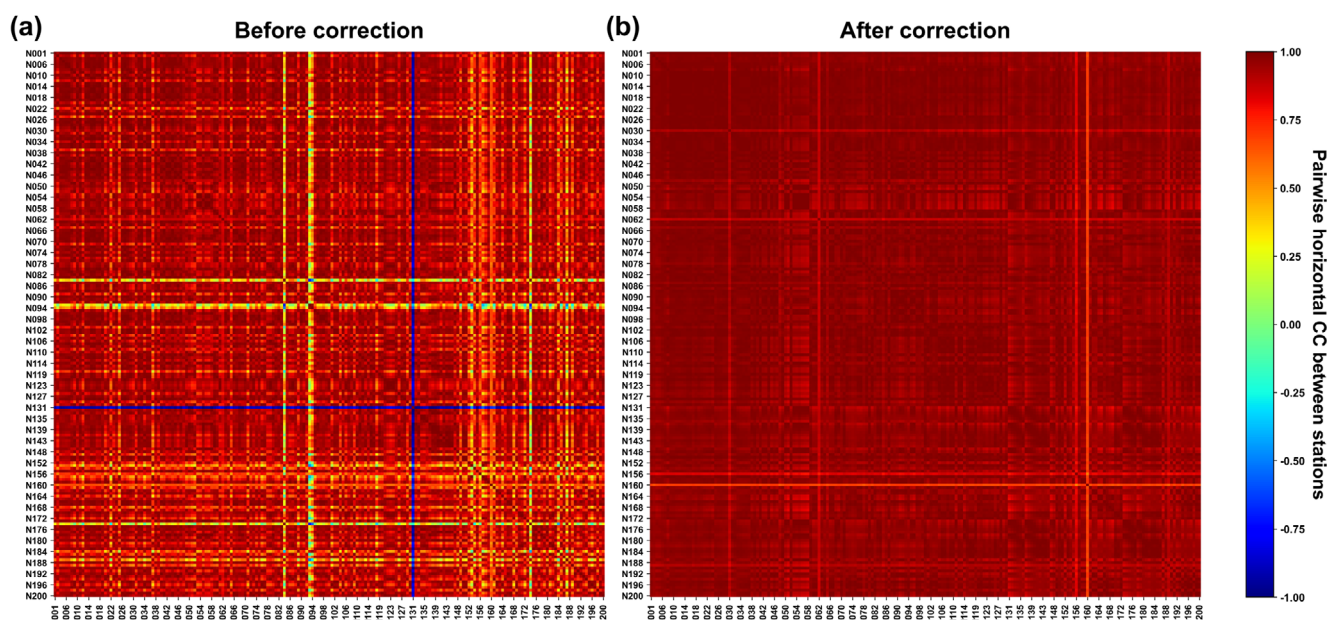
| Event no. | Origin time (UTC)   | Latitude (°) | Longitude (°) | Depth (km) | Magnitude ( $M_W$ ) |
|-----------|---------------------|--------------|---------------|------------|---------------------|
| 1         | 2020-07-22 06:12:44 | 55.0298      | -158.5217     | 28.00      | 7.8                 |
| 2         | 2020-10-19 20:54:39 | 54.6093      | -159.6519     | 31.08      | 7.6                 |
| 3         | 2021-02-10 13:19:55 | -23.0508     | 171.6570      | 10.00      | 7.7                 |
| 4         | 2021-03-04 19:28:33 | -29.7226     | -177.2791     | 28.94      | 8.1                 |

seismograms recorded from stations in GHBSN. If a teleseismic event with sufficient energy is recorded by two close stations, we would expect high degree of correlation between both vertical and horizontal seismograms of station pair. However, in the presence of misaligned stations, we would expect vertical pairwise correlation to be still high while horizontal pairwise correlation to be considerably deteriorated. Upon such an assumption, we chose four teleseismic earthquakes that occurred during the period of GHBSN operation (Table 1) and calculated the pairwise CC between horizontal seismograms before and after correcting for the misorientation angles. To ensure that the teleseismic waveforms were sufficiently similar for every station pair, we applied zero-phase band-pass filter at the frequency range of 0.01–0.05 Hz and used the signals from 100 s before  $T_p$  to 2400 s after the origin time. Moreover, we corrected for the delay time between seismograms from two stations by measuring CC between vertical seismograms which are not affected by sensor misorientation. After that, we calculated the CC between radial components ( $CC_R$ ) and the CC between transverse components

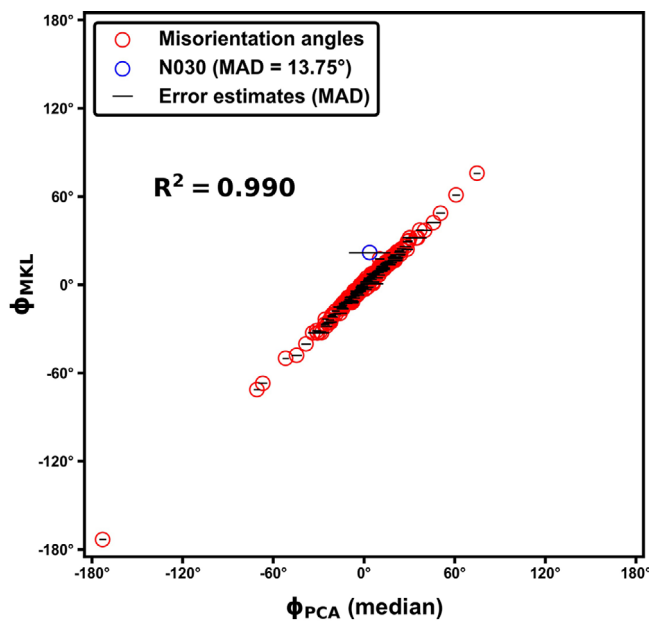
( $CC_T$ ). We took the average of  $CC_R$  and  $CC_T$  as a measure of horizontal pairwise correlation.

Figure 8 shows results of horizontal pairwise correlation for the event 3 (Table 1). We clearly observe that the overall pairwise correlation significantly improved after misorientation correction. Mean pairwise correlation is 0.83 before correction but increased to 0.96 after correction. Similar improvements were also obtained for the other three events (Table 1) (see Figs. S3–S5 in the electronic supplementary material).

We further found the best misorientation angle for each station by searching for the rotation angle which yields maximum horizontal pairwise correlation between each GHBSN station and the permanent station MKL of the KG network (Fig. 1a) whose orientation was previously determined by Son et al. (2021) as  $-16.57^\circ$ . Figure 9 shows the comparison of the misorientations from the correlation-based method using the event 3 (Table 1) and the median misorientations estimated from the  $P_{PCA}$  method. Correlation between the estimates from two methods are high ( $R^2 = 0.990$ ), except for the station N030 (Fig. 1a). However,



**Fig. 8.** Pairwise horizontal CC between 197 stations calculated (a) before misorientation correction and (b) after misorientation correction. We observe that large portion of station pairs with the low CC values were removed after the correction. Event 3 in Table 1 was used for CC calculation.



**Fig. 9.** Comparison of the median misorientation estimates from the  $P_{PCA}$  method ( $\phi_{PCA}$ ) and the misorientation estimates from the correlation-based method applied with MKL station of KG network (Fig. 1a) and event 3 (Table 1) ( $\phi_{MKL}$ ). There exists a high correlation ( $R^2 = 0.990$ ) between  $\phi_{PCA}$  and  $\phi_{MKL}$ . Misorientation estimate of station N030 (Fig. 1a) is marked as a blue circle. The misfit between  $\phi_{PCA}$  and  $\phi_{MKL}$  is quite large for N030 but can be attributed to the relatively large uncertainty (MAD = 13.75°) of  $\phi_{PCA}$ .

considering the relatively large uncertainty for N030 (MAD = 13.75°), the results from two methods can be regarded to be highly consistent. Similar results were obtained by using the three other events from different periods (Fig. S6 in the electronic supplementary material). This analysis demonstrates that correlation-based approach can be useful to rapidly assess misorientation angles if permanent station with well-known orientation exists within or in the vicinity of the array.

### 5.3. Effect of Misorientation Correction on the Teleseismic Receiver Functions

We investigated how our measurement of misorientation angles can enhance the quality of the teleseismic receiver function (RF). The RF provides the signature of seismic discontinuities and information about the S-wave velocity distribution beneath the station. It has been previously suggested that rotation of the sensor can significantly affect the quality of the RF, particularly the tangential component (Lim et al., 2018). Based on our measurement, we accounted for the misorientation when converting the coordinates from vertical-north-east (ZNE) system to vertical-radial-tangential (ZRT) system and examined the effect of misorientation correction on computed radial- and tangential-component RFs (R-RF and T-RF, respectively).

For the test, we selected 16 stations whose absolute values of measured misorientation angle were exceeded 30° and had not experienced the temporal change in misorientation angle throughout the study period (Fig. 1a). To calculate R-RFs and T-RFs for each station, we followed the procedure described in Lim et al. (2018). We chose the teleseismic earthquakes such that the  $M_W$  is greater than or equal to 5.5 and the epicentral distance is between 30° and 90° with respect to a location of 36.5°N, 128°E (Fig. S7 in the electronic supplementary material). Since low SNR can deteriorate the quality of RFs, we filtered waveforms using a bandpass filter from 0.02 to 2.0 Hz, discarded the waveforms whose three-component average SNR was lower than 2, and also manually checked each waveform to ensure that only the waveforms with clear  $P$ -wave arrivals were left for the analysis. The SNR was calculated based on the window determined in Section 4.1.

Following the procedure used in Lim et al. (2018), we first cut each waveform from 30 s before to 180 s after the theoretical  $P$ -wave arrival time predicted with IASP91. We then converted the coordinate system from the ZNE to ZRT. In this step, we considered two cases: a case with no misorientation correction and a case accounting for the correction. Finally, we deconvolved vertical components from radial and tangential components to compute R-RFs and T-RFs, respectively. We applied frequency domain water-level deconvolution (Langston, 1979) with the water level of  $10^{-2}$  and the Gaussian pulse with a half-width ( $1\sigma$ ) of 2.5 Hz.

The stacked R-RFs and T-RFs with and without the misorientation correction for all 16 stations are shown in Figure 10. Prior to stacking, each individual RF was cut to 3 s before and after the  $P$ -wave onset and was normalized to the maximum absolute amplitude. Except for the station N131 showing almost opposite polarity of R-RFs before and after the correction, misorientation correction has only minimal effect on R-RFs within the considered time window. However, the effect of correction on T-RFs is quite remarkable. In principle, the amplitudes of T-RFs at 0 s should be zero. Nonetheless, significant peaks at/near 0 s are observed for the T-RFs calculated without the correction. In contrast, the corrected T-RFs display nearly zero amplitude at 0 s for all the examined stations. This result clearly demonstrates that the misorientation correction is required to be proceeded in prior to RF calculation for better interpretation of both R- and T-RFs. In particular, the correction can be an important procedure to undertake when computing T-RFs as they provide useful constraints on the anisotropic and dipping structures beneath the receiver (Park and Levin, 2016; Lim et al., 2018). The effect of misorientation correction can also be observed from the back-azimuthal record section of R-RFs and T-RFs (Fig. S8 in the electronic supplementary material).

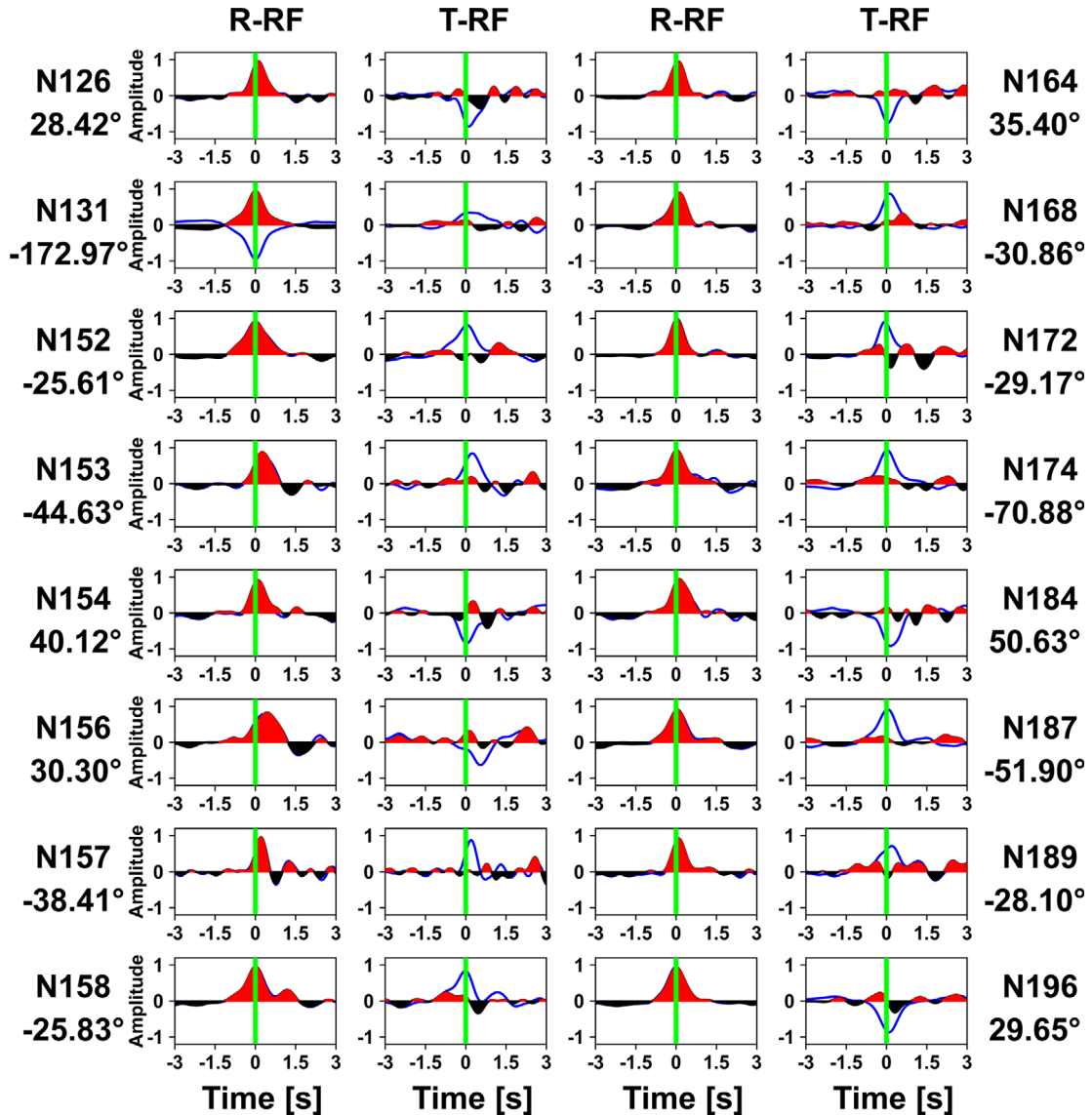


**Fig. 10.** Comparison of R-RFs and T-RFs calculated for 16 selected stations (Fig. 1a) before and after the misorientation correction. The RFs calculated before correction are shown as blue curves. The RFs calculated after correction are shown as the curves whose positive and negative areas between x-axes and them are filled with red and black colors, respectively. Green vertical lines mark 0 s. The station name and the corresponding misorientation angle are annotated beside each RF plot.

## 6. CONCLUSIONS

We estimated time-dependent misorientation angles of 200 stations in GHBSN based on computationally-efficient  $P$ -wave polarization methods. Two different methods ( $P_{PCA}$  and  $P_{min\ T}$ ) provided highly consistent results ( $R^2 > 0.999$ ) and overall uncertainty level was very low (average MAD of  $3.14^\circ$ ). Referring to field operation record, we demonstrated that our measurements are generally robust and can provide additional changes in sensor alignment that were not reported. By calculating the interstation cross-correlation between horizontal-component seismograms of teleseismic events before and after misorientation correction, we showed that the overall correlation between station pairs

significantly improved after correction. We also verified that correcting for our sensor misorientation angles effectively minimizes the energy in T-RFs at 0 s. Our misorientation measurements are not restricted to particular period, but available for the full deployment history which permits researchers to use data from any period. We expect our measurements to serve as a crucial metadata for performing seismological researches utilizing three-component GHBSN data.

## DATA AND RESOURCES

The organizations responsible for deploying and managing the GHBSN are Korea Institute of Nuclear Safety, Korea University,

Pukyong National University, and Seoul National University. The earthquake catalog used in this research is obtained from IRIS DMC FDSNWS event web service (<https://ds.iris.edu/ds/nodes/dmc/data/types/events/catalogs/>). All the data were last accessed in April 2021. We used *ObsPy* (<https://github.com/obspy/obspy/wiki/>) for processing seismic waveform data. Change point detection by PELT was performed using a Python library *ruptures* (<https://centre-borelli.github.io/ruptures-docs/>). Receiver function analysis was performed using a Python library *rf* (<https://rf.readthedocs.io/en/latest/>).

## ACKNOWLEDGMENTS

This work was supported by SNU Student-directed Education Undergraduate Research Program through the Faculty of Liberal Education, Seoul National University (2020). The authors thank W.-Y. Kim, H. Lim and H. Kang in Seoul National University for constructive suggestions which improved the quality of the work. Authors acknowledge support from the Nuclear Safety Research Program through the Korea Foundation of Nuclear Safety (KoFONS), granted financial resource from the Nuclear Safety and Security Commission (NSSC), Republic of Korea (No. 1705010). Y. Kim acknowledges support from Creative-Pioneering Researchers Program through Seoul National University (SNU SRnD 3345-20160014). Finally, the authors thank Guest Editor, Dong-Hoon Sheen, and two anonymous reviewers for comments which greatly improved this paper.

## REFERENCES

- Braunmiller, J., Nabelek, J., and Ghods, A., 2020, Sensor orientation of Iranian broadband seismic stations from *P*-wave particle motion. *Seismological Research Letters*, 91, 1660–1671.
- Büyükkapınar, P., Aktar, M., Maria Petersen, G., and Köseoğlu, A., 2021, Orientations of broadband stations of the KOERI seismic network (Turkey) from two independent methods: *P*- and Rayleigh-wave polarization. *Seismological Research Letters*, 92, 1512–1521.
- Doran, A.K. and Laske, G., 2017, Ocean-bottom seismometer instrument orientations via automated Rayleigh-wave arrival-angle measurements. *Bulletin of the Seismological Society of America*, 107, 691–708.
- Eisermann, A.S., Ziv, A., and Wust-Bloch, G.H., 2015, Real-time back azimuth for earthquake early warning. *Bulletin of the Seismological Society of America*, 105, 2274–2285.
- Ekström, G. and Busby, R.W., 2008, Measurements of seismometer orientation at USArray transportable array and backbone stations. *Seismological Research Letters*, 79, 554–561.
- Ekström, G. and Nettles, M., 2018, Observations of seismometer calibration and orientation at USArray stations, 2006–2015. *Bulletin of the Seismological Society of America*, 108, 2008–2021.
- Ensing, J.X. and van Wijk, K., 2018, Estimating the orientation of borehole seismometers from ambient seismic noise. *Bulletin of the Seismological Society of America*, 109, 424–432.
- Harris, C.R., Millman, K.J., van der Walt, S.J., Gommers, R., Virtanen, P., Cournapeau, D., Wieser, E., Taylor, J., Berg, S., Smith, N.J., Kern, R., Picus, M., Hoyer, S., van Kerkwijk, M.H., Brett, M., Haldane, A., del Rio, J.F., Wiebe, M., Peterson, P., Gérard-Marchant, P., Shepard, K., Reddy, T., Weckesser, W., Abbasi, H., Gohlke, C., and Oliphant, T.E., 2020, Array programming with NumPy. *Nature*, 585, 357–362.
- Jurkevics, A., 1988, Polarization analysis of three-component array data. *Bulletin of the Seismological Society of America*, 78, 1725–1743.
- Kennett, B.L.N. and Engdahl, E.R., 1991, Traveltimes for global earthquake location and phase identification. *Geophysical Journal International*, 105, 429–465.
- Killick, R., Fearnhead, P., and Eckley, I.A., 2012, Optimal detection of changepoints with a linear computational cost. *Journal of the American Statistical Association*, 107, 1590–1598.
- Kim, W.-Y., Choi, H., and Noh, M., 2010, The 20 January 2007 Odae-san, Korea, earthquake sequence: reactivation of a buried strike-slip fault? *Bulletin of the Seismological Society of America*, 100, 1120–1137.
- Kim, Y., He, X., Ni, S., Lim, H., and Park, S.C., 2017, Earthquake source mechanism and rupture directivity of the 12 September 2016  $M_W$  5.5 Gyeongju, South Korea, earthquake. *Bulletin of the Seismological Society of America*, 107, 2525–2531.
- Langston, C.A., 1979, Structure under Mount Rainier, Washington, inferred from teleseismic body waves. *Journal of Geophysical Research: Solid Earth*, 84, 4749–4762.
- Laske, G., Masters, G., and Zu, W., 1994, Frequency-dependent polarization measurements of long-period surface waves and their implications for global phase-velocity maps. *Physics of the Earth and Planetary Interiors*, 84, 111–137.
- Lee, H. and Sheen, D.H., 2015, A study on determination of orientation of borehole seismometer. *Journal of the Geological Society of Korea*, 51, 93–103.
- Lee, S.J. and Rhie, J., 2015, Determining the orientations of broadband stations in South Korea using ambient noise cross-correlation. *Geophysics and Geophysical Exploration*, 18, 85–90.
- Lim, H., Kim, Y., Kwon, K.B., Han, J., Ahn, B.S., Chai, G., Choi, Y., Heo, D., Jung, Y., Kang, H., Koh, M.H., Kwon, J., Park, J.Y., Seo, M.-S., Son, Y.O., Han, S., Kang, T.-S., Rhie, J., Kim, K.-H., and Ree, J.-H., 2021, Deployment of the linear array with geophones on the fault zone of the 2016  $M_W$  5.5 Gyeongju earthquake. *Journal of the Geological Society of Korea*, 57, 741–746.
- Lim, H., Kim, Y., Song, T.R.A., and Shen, X., 2018, Measurement of seismometer orientation using the tangential *P*-wave receiver function based on harmonic decomposition. *Geophysical Journal International*, 212, 1747–1765.
- Liu, K.H. and Gao, S.S., 2013, Making reliable shear-wave splitting measurements. *Bulletin of the Seismological Society of America*, 103, 2680–2693.
- Niu, F. and Li, J., 2011, Component azimuths of the CEArray stations estimated from *P*-wave particle motion. *Earthquake Science*, 24, 3–13.
- Ojo, A.O., Zhao, L., and Wang, X., 2019, Estimations of sensor misorientation for broadband seismic stations in and around Africa. *Seismological Research Letters*, 90, 2188–2204.

- Park, J. and Levin, V., 2016, Anisotropic shear zones revealed by backazimuthal harmonics of teleseismic receiver functions. *Geophysical Journal International*, 207, 1216–1243.
- Pearson, K., 1901, Principal components analysis. *The London, Edinburgh, and Dublin Philosophical Magazine and Journal of Science*, 6, 559–572.
- Rueda, J. and Mezcua, J., 2015, Orientation analysis of the Spanish Broadband National Network using Rayleigh-wave polarization. *Seismological Research Letters*, 86, 929–940.
- Scholz, J.R., Barruol, G., Fontaine, F.R., Sigloch, K., Crawford, W., and Deen, M., 2017, Orienting ocean-bottom seismometers from *P*-wave and Rayleigh wave polarisations. *Geophysical Journal International*, 208, 1277–1289.
- Shen, X., Kim, Y., Song, T.R.A., and Lim, H., 2019, Data-oriented constraint on the interpretation of S receiver function and its application to observations of seismic discontinuities in the lithosphere–asthenosphere system. *Geophysical Journal International*, 219, 496–513.
- Shin, J.S., Sheen, D.H., and Shin, I.C., 2009, Orientation correction for borehole seismic stations in South Korea. *Journal of the Geological Society of Korea*, 45, 47–54.
- Son, Y.O., Seo, M.-S., and Kim, Y., 2021, Measurement of seismometer misorientation based on *P*-wave polarization: application to permanent seismic network in South Korea. *Geosciences Journal*. <https://doi.org/10.1007/s12303-021-0031-5>
- Stachnik, J.C., Sheehan, A.F., Zietlow, D.W., Yang, Z., Collins, J., and Ferris, A., 2012, Determination of New Zealand ocean bottom seismometer orientation via Rayleigh-wave polarization. *Seismological Research Letters*, 83, 704–713.
- Wang, X., Chen, Q.F., Li, J., and Wei, S., 2016, Seismic sensor misorientation measurement using *P*-wave particle motion: an application to the NECsaids Array. *Seismological Research Letters*, 87, 901–911.
- Woo, J.U., Rhie, J., Kim, S., Kang, T.-S., Kim, K.-H., and Kim, Y., 2019, The 2016 Gyeongju earthquake sequence revisited: aftershock interactions within a complex fault system. *Geophysical Journal International*, 217, 58–74.
- Xu, H., Luo, Y., Tang, C.C., Zhao, K., Xie, J., and Yang, X., 2018, Systemic comparison of seismometer horizontal orientations based on teleseismic earthquakes and ambient-noise data. *Bulletin of the Seismological Society of America*, 108, 3576–3589.
- Xu, W., Yuan, S., Wang, W., Luo, X., and Li, L., 2020, Comparing orientation analysis methods for a shallow-water ocean-bottom seismometer array in the Bohai Sea, China. *Bulletin of the Seismological Society of America*, 110, 3174–3184.
- Zahradník, J. and Custódio, S., 2012, Moment tensor resolvability: application to southwest Iberia. *Bulletin of the Seismological Society of America*, 102, 1235–1254.
- Zeng, S., Zheng, Y., Niu, F., and Ai, S., 2020, Measurements of seismometer orientation of the first phase CHINArray and their implications on vector-recording-based seismic studies. *Bulletin of the Seismological Society of America*, 111, 36–49.
- Zha, Y., Webb, S.C., and Menke, W., 2013, Determining the orientations of ocean bottom seismometers using ambient noise correlation. *Geophysical Research Letters*, 40, 3585–3590.
- Zheng, H., Fan, J., Zhao, D., Li, C., Dong, D., Zhang, G., and Wang, X., 2020, A new method to estimate ocean-bottom-seismometer orientation using teleseismic receiver functions. *Geophysical Journal International*, 221, 893–904.
- Zhu, G., Yang, H., Lin, J., and You, Q., 2020, Determining the orientation of ocean-bottom seismometers on the seafloor and correcting for polarity flipping via polarization analysis and waveform modeling. *Seismological Research Letters*, 91, 814–825.

**Publisher's Note** Springer Nature remains neutral with regard to jurisdictional claims in published maps and institutional affiliations.